Acta Materialia 98 (2015) 275–287

Contents lists available at ScienceDirect

Acta Materialia

journal homepage: www.elsevier.com/locate/actamat

Influence of a microalloying addition of Ag on the precipitation kinetics of an Al–Cu–Mg alloy with high Mg:Cu ratio

C. Macchi [a,b], A. Tolley [c,b,*], R. Giovachini [a], I.J. Polmear [d], A. Somoza [a,e]

[a] Instituto de Física de Materiales Tandil, CIFICEN (CONICET-UNCPBA), Pinto 399, B7000GHG Tandil, Argentina
[b] Consejo Nacional de Investigaciones Científicas y Técnicas (CONICET), Argentina
[c] Centro Atómico Bariloche, Comisión Nacional de Energía Atómica, Avda. Bustillo 9500, R8400AGQ San Carlos de Bariloche, Argentina
[d] Department of Materials Engineering, Monash University, Melbourne, Vic. 3800, Australia
[e] Comisión de Investigaciones Científicas de la Provincia de Buenos Aires (CICPBA), Argentina

ARTICLE INFO

Article history:
Received 11 May 2015
Revised 7 July 2015
Accepted 11 July 2015
Available online 23 July 2015

Keywords:
Age-hardenable alloys
Precipitation
Transmission electron microscopy
Positron annihilation spectroscopy

ABSTRACT

Effects of microalloying with Ag on the precipitation process in an Al–Cu–Mg alloy with high Mg:Cu ratio have been investigated during artificial ageing of the ternary and quaternary compositions Al–1.5 wt.%Cu–4 wt.%Mg(–0.5 wt.%Ag) at 175 °C, combining transmission electron microscopy and positron lifetime spectroscopy. In addition, coincidence Doppler broadening of the positron–electron annihilation radiation was used to provide information about the chemical environment surrounding vacancy-like defects. The results obtained for the silver-free alloy indicate that, immediately after quenching from the solution treatment temperature, vacancy v-Cu–Mg clusters are formed in the supersaturated solid solution. During the early stages of ageing these clusters become richer in Cu and Mg and laths of the *S* phase (Al_2CuMg) nucleate preferentially on dislocation lines. Continued ageing led to gradual precipitation of an equi-axed phase in the matrix between the *S* phase laths which is believed to be the cubic *Z* phase thought previously to form only if silver is present. For the silver-containing Al–Cu–Mg alloy, v-Cu–Mg–Ag aggregates also form immediately after quenching and the solute transport mechanisms are the same. However, precipitation of the *S* phase is suppressed during ageing and the silver addition promotes accelerated formation of a finer dispersion of smaller equi-axed *Z* phase precipitates. For both alloys, no evidence was found that the *Z* phase is preceded by any pre-precipitate or GP zones. Combination of coincidence Doppler broadening and microanalysis results revealed the *Z* phase to have a Mg:Cu ratio of 2 which indicates that it differs from the well known *T* phase (Al_6CuMg_4) which the equilibrium phase diagram indicates should form in Al–Cu–Mg alloys with high Mg:Cu ratios. Additional ageing experiments at 240 °C showed that neither the *Z* phase or *T* phase are formed in the ternary alloy, but only precipitates of the *S* phase, while in the quaternary alloy the *S* phase is strongly suppressed and mainly *Z* phase precipitates are formed.

1. Introduction

The phenomenon of age hardening was first discovered in the alloy Al–3.5%Cu–0.5%Mg–0.5%Mn (wt.%) by Wilm in 1906 [1]. Since then the Al–Cu–Mg system has been the basis for most of the important 2000 series of high strength aluminum alloys which have compositions that place them in the ($\alpha + S$) region of the ternary phase diagram (Fig. 1) [2]. One characteristic of all these alloys is that, when they are aged at elevated temperatures (~100–240 °C), hardening occurs in two distinct stages separated by a plateau during which the hardness may remain constant for many hours [3–6]. Another special feature is that the first ageing stage, which may account for as much as 70% of the total hardening, occurs rapidly and may be complete after ageing for only 60 s [5,6].

Earlier classical X-ray diffraction studies of precipitation processes in ternary Al–Cu–Mg alloys concluded that the first stage of hardening is associated with the formation of Guinier–Preston (Cu, Mg) zones (also known commonly as GPB zones) [7,8]. However, later studies by Ringer et al. [6,9] involving high resolution electron microscopy, electron diffraction and atom probe field ion microscopy, failed to detect the presence of GPB zones during the first stage of ageing. Instead, they attributed the rapid early hardening to the formation of solute atom/vacancy clusters and have termed this phenomenon *cluster hardening*. Furthermore,

* Corresponding author at: Centro Atómico Bariloche, Comisión Nacional de Energía Atómica, Avda. Bustillo 9500, R8400AGQ San Carlos de Bariloche, Argentina.
E-mail address: tolley@cab.cnea.gov.ar (A. Tolley).

http://dx.doi.org/10.1016/j.actamat.2015.07.032
1359-6454/

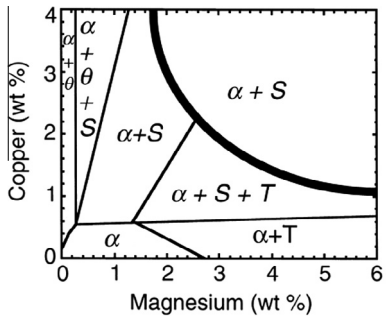

Fig. 1. Aluminum-rich corner of the Al–Cu–Mg phase diagram indicating the phases present as a function of composition, after long term ageing at 190 °C [2].

these workers also claimed that GPB zones were not formed until ageing had proceeded towards the end of the hardness plateaus in the respective hardness/time curves.

Heterogeneous nucleation of laths of the orthorhombic S phase (Al_2CuMg), or its closely similar metastable form S', also occurs on dislocation lines early in the ageing process and these laths increase in size as ageing proceeds along the hardness plateau [10–12]. The second stage of hardening has been attributed to the combined presence of these GPB zones and the S' and/or S phases [6,8] although a second type of GP zone structure [8], and another metastable phase S'' [13,14], have been reported to contribute to hardening at high ageing temperatures (e.g., 240 °C).

Another interesting feature of age hardening in a wide range of compositions based on the Al–Cu–Mg system is that micro-additions of silver (e.g., 0.1 at.%) have been shown both to accelerate ageing and to stimulate an increased response to age hardening [4,5,15]. Furthermore, depending on the Mg:Cu ratios of the alloys, silver has been found to promote formation of three new precipitates that are described below.

Special attention has been paid to Al–Cu–Mg–Ag alloys with low Mg:Cu ratios that lie in the ($\alpha + S + \theta$) region of ternary phase diagram, and in which silver has been found to stimulate formation of a face-centered orthorhombic phase, designated Ω [16–18]. This phase nucleates at the sites of v-Mg–Ag co-clusters that form immediately elevated temperature ageing has commenced [19–21], after which it precipitates as a fine dispersion of thin plates along the $\{1\,1\,1\}_\alpha$ planes. Ω is closely related to the tetragonal phase θ (Al_2Cu) that forms on the {1 0 0} planes in aged binary Al–Cu alloys [20]. During the growth of Ω, all the Ag and Mg atoms appear to partition to the Ω/matrix interfaces which has been shown to promote coherency along the $\{1\,1\,1\}_\alpha$ planes [22–24]. Because of this, Al–Cu–Mg–Ag alloys hardened by the Ω phase may show high levels of strength (e.g., 0.2% proof stress 480 MPa) and exhibit creep properties that are superior to existing commercial 2000 alloys [25–26].

For Al–Cu–Mg alloys with higher magnesium contents (i.e., higher Mg:Cu ratios) that lie in the ($\alpha + S$) region of the ternary phase diagram, silver promotes formation of a close packed hexagonal phase [6,27], designated X', which also nucleates at the sites of Mg–Ag co-clusters. These quaternary alloys also have much shorter hardness plateaus when aged at elevated temperatures [5,6] and the second stage of hardening is considered to originate from the combined presence of GPB zones, X', and possibly fine particles of the S phase [6]. Atom probe analysis indicates that the composition of X' approximates to that of the S phase (Al_2CuMg) except that it also contains the silver addition in solid solution [6].

Little commercial interest has been shown in Al–Cu–Mg alloys with relatively high magnesium contents (i.e., even higher Mg:Cu ratios) that lie in the ($\alpha + S + T$) region of the ternary phase diagram. Here the T phase has been shown to have a complex body-centered cubic unit cell with $a_o = 1.425$ nm and has the approximate composition Al_6CuMg_4 [28,29]. Once again it has been demonstrated that micro-additions of silver to these alloys promotes an increased response to age hardening at elevated temperatures [5]. At first this behavior was attributed to silver stimulating precipitation of a finely dispersed and slightly modified, metastable version of the T phase [5,15,30]. However, more recent convergent-beam electron diffraction studies have indicated that hardening is associated, at least in part, with precipitation of a new phase, designated Z, which has a face-centered cubic unit cell with $a_o = 1.999$ nm. [31]. This work has also revealed that the Z phase has two variants which form on the $\{1\,1\,0\}_\alpha$ and $\{1\,1\,1\}_\alpha$ planes, respectively, with the latter becoming dominant as ageing is continued.

Additional valuable information about the role of vacancies in precipitation processes in aged aluminum alloys can be obtained using positron annihilation spectroscopy (PAS) which relies of the propensity of positrons to be trapped by open volumes inside solids (vacancy-like defects). Because of this, positron annihilation lifetime spectroscopy (PALS) is proving to be the most sensitive experimental technique for observing vacancy-like defects and the role they play during structural transformations in alloys [32,33]. Another variant of PAS called coincidence Doppler broadening (CDB) spectroscopy has also proved to be particularly useful for identifying the nature of the solute atoms in contact with vacancy-like defects in precipitates [34–38]. Both these positron techniques have been successfully applied to investigate precipitation reactions in several ternary Al–Cu–Mg alloys and in the related commercial alloy 2024 [21,39–43]. Furthermore, PALS has contributed to the understanding of the effects of adding a micro-addition of silver on the precipitation process in the alloy Al–4%Cu–0.3%Mg which has a low Mg:Cu ratio [21].

The present investigation was undertaken to obtain an increased understanding of the precipitation mechanisms involved when silver-free and silver-containing Al–Cu–Mg alloys with high magnesium contents that lie in the ($\alpha + S + T$) region of the phase diagram are age hardened at elevated temperatures. The alloys investigated were Al–1.5%Cu–4%Mg (wt.%) with and without 0.5%Ag (wt.%). Microstructural characterization of both alloys was carried out using transmission electron microscopy (TEM) and high resolution electron microscopy (HRTEM) in order to interpret the evolution of hardness changes and positron lifetimes occurring during elevated temperature ageing. These observations were complemented with CDB spectroscopy to provide information about the chemical environment surrounding the positron traps.

2. Experimental procedures

2.1. Alloy preparation and thermal treatment

The composition of the alloys studied in this work was: (i) ternary alloy VE: Al–1.5%Cu–4%Mg (wt.%); and (ii) quaternary alloy VEA: Al–1.5%Cu–4%Mg–0.5%Ag (wt.%). The two alloys were prepared using high purity metals and hot rolled to produce 1.5 mm thick sheets. Specimens were solution treated at 520 ± 3 °C for 6 h in an air circulating electrical furnace and quenched in water at 20 °C. After quenching, samples for combined TEM, hardness, PALS and CDB characterization were artificially aged in a glycerin bath at 175 °C, for various times and again quenched into cold water. This ageing temperature was chosen in order to reach peak ageing in reasonable experimental times (see Ref. [5]). In addition, specimens for TEM characterization were artificially aged at 240 °C for 240 h or more immediately after quenching. This ageing

temperature is the one used by Chopra et al. [31] in studying the same Ag-containing Al–Cu–Mg alloy.

Samples for PALS, CDB and hardness measurements ($10 \times 10 \times 1.5\ mm^3$) were spark machined from the sheets and grounded mechanically with emery paper and ending with 1 μm diamond paste to remove the damage introduced in this process.

2.2. Positron annihilation lifetime spectroscopy and hardness testing

PALS spectra were obtained at RT using a standard fast–fast lifetime spectrometer which had a resolution of 255 ps and a count rate of 200 s^{-1} circa. A 0.74 MBq sealed source of ^{22}NaCl deposited onto two Kapton foils (7.5 μm thick) was sandwiched between two identical alloy specimens. PALS spectra with about 2.5×10^6 coincidence counts were collected and the lifetime spectra were deconvoluted through the POSITRONFIT program [44]. The lifetime value of positrons annihilated in Kapton foils is well-known, 382 ps, and its associated intensity was 11%. This fraction value was determined from the decomposition of lifetime spectra for well-annealed pure Al (99.999% purity). After subtraction of the source component, the spectra were analyzed as one exponential lifetime component. Since the spectra were expected to contain two or more unresolved components, the resultant one-component fits must be accepted as an effective average lifetime.

Vickers microhardness measurements, using a load of 100 g and a loading time of 10 s, were performed at RT after each positron lifetime measurement had been made in order to compare the respective age hardening behavior of the two alloys.

2.3. Coincidence Doppler broadening of the annihilation radiation

All measurements were taken at RT by means of two hyperpure Ge gamma detectors (90% of relative efficiency for the ^{60}Co line at 1.33 MeV) coupled to a multiparametric pulse analyzer. The samples were arranged in the usual sample-source-sample sandwich geometry. Background rejection was achieved by requiring time coincidence within a window of 300 ns and fulfillment of the energy conservation condition $|E_1 + E_2 - 2m_0c^2| < 2.1$ keV, where E_1 and E_2 are the energies measured by the two detectors, respectively. The component along the axis joining the two detectors of the momentum of the annihilating pairs is given by $p_L = \frac{E_1 - E_2}{c}$.

The resolution of the CDB spectrometer was 1.1 keV estimated at 511 keV. Ten million counts were collected in each spectrum. The analysis of the momentum spectra ρ was carried out, as explained in Refs. [36,43], by fitting a linear combination of momentum spectra measured in the same experimental condition for pure elements, as given by the following function:

$$\rho_{fit} = (1 - F_{trap})\rho_{Al}^{bulk} + F_{trap}\left(C_{Al}^{v}\rho_{Al}^{v} + C_{Mg}^{v}\rho_{Mg}^{v} + C_{Cu}^{v}\rho_{Cu}^{v} + C_{Ag}^{v}\rho_{Ag}^{v}\right), \quad (1)$$

where the fitting parameters are the trapping fraction F_{trap} (relative number of positrons that are trapped and annihilated in vacancy-like defects) and the fractional concentrations C_{Al}^{v}, C_{Cu}^{v}, C_{Mg}^{v}, and C_{Ag}^{v} (for alloy VE in Eq. (1) $C_{Ag}^{v} = 0$). It should be noted that the fractional concentrations C_i^v are to be interpreted as representing (with a possible distortion, due to the different positron affinity for the different elements [35] and to the lattice relaxation) the atomic composition in regions that are in immediate contact with the vacancy where the positron is trapped. It must be emphasized that the local composition in contact with a defect can differ from the average composition of the vacancy–solute aggregates. In Eq. (1), ρ_{Al}^{bulk} is the momentum distribution for free positrons annihilating in the alloy matrix. In the present work, this momentum distribution will be considered as that of Al, since the sensitivity of positrons to a small percentage of substitutional impurities in a supersaturated solid solution can be neglected. Consequently, ρ_{Al}^{bulk} is the experimental momentum distribution measured in well-annealed pure Al; ρ_{Al}^{v}, ρ_{Mg}^{v}, ρ_{Cud}^{v}, ρ_{Ag}^{v} are the momentum distributions expected for annihilation in vacancy-like defects in pure elements, as obtained from measurements on severely cold worked samples after subtracting the contribution of annihilations with free positrons [38].

The momentum spectra ρ of the annihilation radiation are usually presented in terms of the ratio CDB differences curves relative to a reference material (named Δ curves), in our case we have used well-annealed pure Al:

$$\Delta = \frac{\rho - \rho_{Al}^{bulk}}{\rho_{Al}^{bulk}}, \quad (2)$$

where ρ_{Al}^{bulk} is the CDB spectrum measured for bulk Al (i.e., well-annealed pure Al). This representation is used to enhance the details of the spectra in the high-momentum region, which is most important for the identification of the chemical species in contact with vacancy-like defects [36,43]. The symmetrical experimental curves have been folded around $p_L = 0$. The statistical noise has been reduced by averaging groups of three subsequent points from about 0.7 to 1.4 atomic momentum units and of six points above 1.4 atomic units.

In Fig. 2, in the form of relative difference curves Δ to bulk Al, we show the reference momentum spectra obtained for pure well-annealed Al, Mg, Cu and Ag. These spectra were obtained under the condition of saturated positron trapping and used as reference spectra when the fitting procedure was applied through Eq. (1).

2.4. Transmission electron microscopy

Microstructural characterization of VE and VEA alloys was carried out using TEM. Alloy samples were prepared by cutting out 3 mm diameter discs from 1.5 mm thick sheets using spark erosion followed by mechanical grinding to a thickness of about 150 μm. Final thinning was carried out by double jet electropolishing using an electrolyte that contained 8% sulfuric acid, 2% hydrofluoric acid, 5% glycerol in methanol at −30 °C and an applied voltage of 17 V.

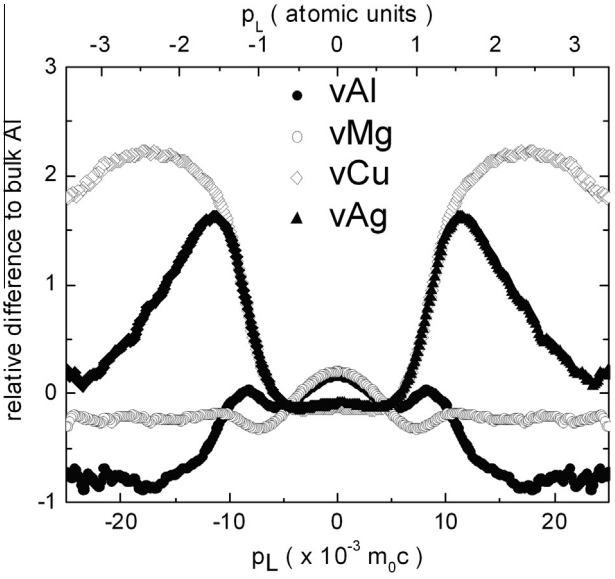

Fig. 2. Reference CDB distributions, relative differences to bulk Al, corresponding to positrons annihilating in vacancy-like defects in Al, Cu, Mg and Ag.

The age hardened specimens were examined with a Philips CM200UT microscope equipped with a Lanthanum hexaboride thermionic cathode and an ultratwin objective lens. Microanalysis of small regions was carried out in a low background specimen holder using an 18 nm diameter beam with an EDAX detector and Genesis software. Prior to examination, plasma-cleaning was used to reduce contamination effects under the action of the electron beam.

3. Experimental results

- VE alloy (Al–1.5%Cu–4%Mg, wt.%).

3.1. Positron annihilation lifetime spectroscopy and hardness testing

Changes in Vickers hardness and positron lifetimes during artificial ageing in alloy VE at 175 °C are shown in Fig. 3. This figure contains the same experimental information previously reported by Macchi et al. [45], but with additional data points included so that a more detailed indication of these property changes could be obtained as a function of ageing time.

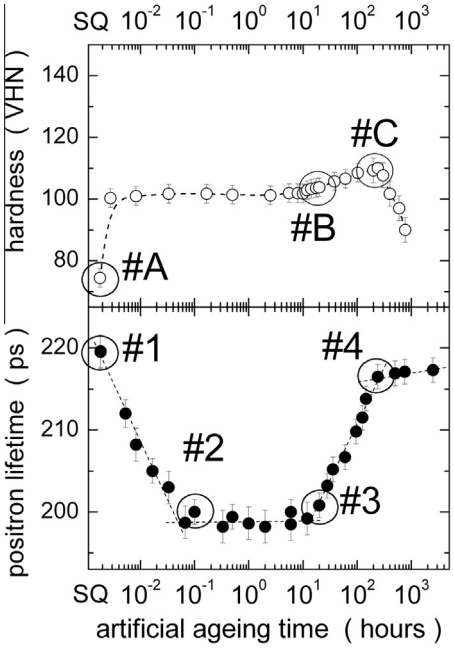

Fig. 3. Evolution during artificial ageing at 175 °C of the Vickers microhardness and positron lifetime for alloy VE (Al–1.5 wt.%Cu–4.0 wt.%Mg). The dotted lines are only eye guides. Labels #A, #B and #C and #1, #2, #3 and #4 represent specific ageing stages selected to obtain TEM and CDB information (see text).

The initial hardness value for the as-quenched specimens was 75 ± 2 VHN; after which it increased rapidly in less than 1 min at 175 °C until it attained a hardness plateau of 100 ± 2 VHN that remained constant for about 24 h. After this, a second increase in hardness occurred until a peak value of 110 ± 2 VHN was observed in approximately 240 h. Further ageing then caused softening as the alloy overaged.

Instead, the positron lifetime rapidly decreased from the value measured in as-quenched samples, around 220, to 199 ± 1 ps within a period of approximately 3 min, after which it remained almost constant for the next 12 h. The positron lifetime then increased again to a value of ~216 ps as ageing was continued to approximately 240 h which corresponded to peak hardness. In the overageing stage, a very slight increment of the positron lifetime was observed.

The circles labeled #A, #B, #C and #D on the hardness/time curve and those #1, #2, #3 and #4 in the lifetime evolution represent specific ageing stages that were selected to obtain additional information by means of TEM and CBD spectroscopy of the positron–electron annihilation radiation.

3.2. Transmission electron microscopy

Fig. 4 compares a series of images of alloy VE after ageing for 20, 120 and 240 h at 175 °C. At 20 h ageing, which approximately corresponds to the end of the plateau of the hardness/time curve, lengths of helical dislocations decorated with *S* phase precipitates were observed. Occasional larger lath shaped *S* phase particles with typical widths and thicknesses of 600 and 50 nm respectively were also observed. What is particularly interesting is that small equi-axed precipitates in the size range 30–50 nm had formed in the matrix between the dislocations in the specimens aged for the longer times. These precipitates were studied in more detail. Fig. 5 compares images from specimens aged for 240 and 1000 h at 175 °C. The mean size of such precipitates increased from 26 ± 1 to 32 ± 1 nm. The morphology of the precipitates was studied by analyzing the projected shape along different orientations, shown in Fig. 6. The particles exhibited a square-shaped projection along the [100] matrix zone axis, with edges parallel to the ⟨110⟩ directions. When imaged along the [011] zone axis, the projected shape was a rhombus, with edges parallel to the {111} planes. Occasionally edges parallel to {002} planes were also observed. When imaged along the [111] zone axis the projected shape was hexagonal. Such projected shapes correspond to octahedral shaped precipitates with principal facets parallel to the {111} matrix planes and occasionally smaller facets parallel to the {002} matrix planes.

Fig. 7 shows selected area diffraction patterns where weak precipitate reflections are observed in between the stronger matrix reflections. The observed reflections are very similar to those

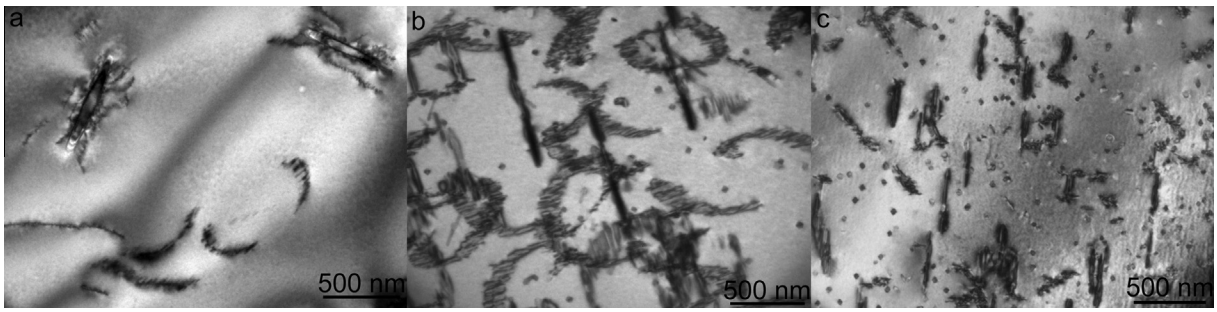

Fig. 4. Evolution of the microstructure of alloy VE during ageing at 175 °C. (a) 20 h; (b) 120 h; (c) 240 h. Small sized equiaxed precipitates can be observed in between dislocations decorated with *S* phase precipitates after 120 and 240 h of ageing.

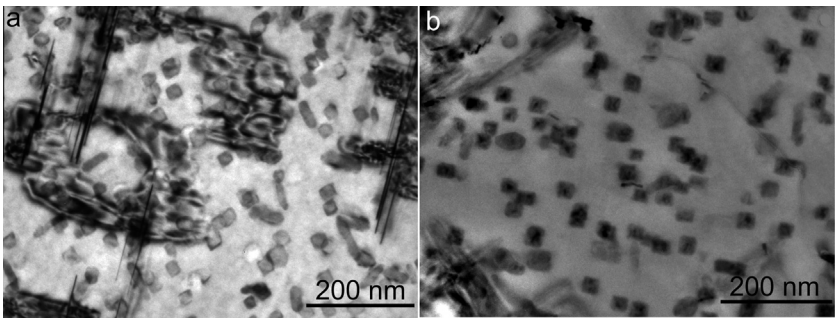

Fig. 5. Comparison of the small equiaxed precipitates in between dislocations after 240 h (a) and 1000 h ageing at 175 °C (b) in alloy VE. Mean sizes were (26 ± 1) nm and (32 ± 1) nm, respectively.

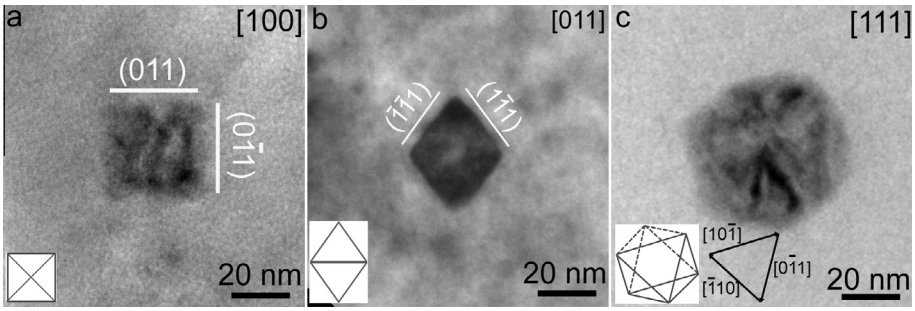

Fig. 6. VE alloy after 240 h at 175 °C: small particles' projected shapes along the 100 (a), 011 (b) and 111 (c) matrix zone axis. The insets show the projected shape of an octahedron with {111} facets.

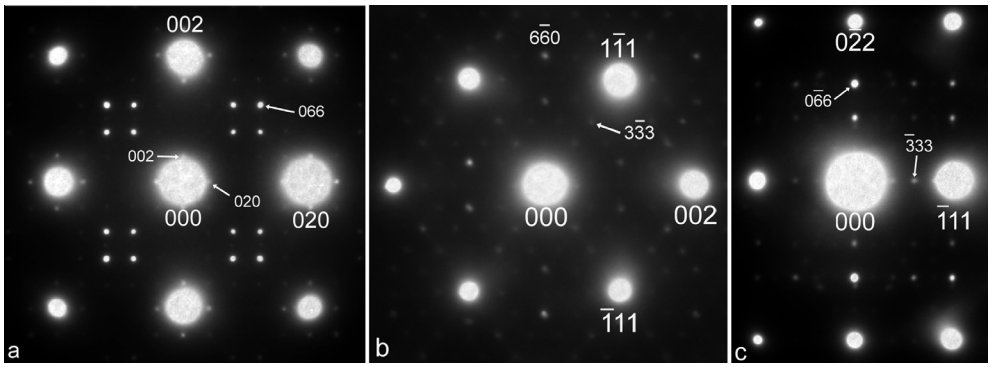

Fig. 7. SAD patterns along (a) [100], (b) [110] and (c) [211] zone axis showing reflections corresponding to the small equiaxed precipitates in VE alloy. The largest indices correspond to the matrix. The smallest indices correspond to the precipitates.

reported by Chopra et al. [31] in the silver containing alloy showing they correspond to what they called the *Z* phase. This phase has a face-centered cubic unit cell, and a cube–cube orientation relationship with the matrix. The *Z* phase reflections are also indexed according to the reported unit cell. Fig. 8 shows a dark field image after 1000 h ageing obtained with a 660 precipitate reflection with the electron beam near to the [100] matrix zone axis. Such kinds of images were used to determine the mean sizes of precipitates reported above after 240 and 1000 h ageing.

Fig. 9 shows a high resolution image obtained along the matrix [110] zone axis, and its corresponding diffractogram, showing spots identical to those of the diffraction pattern in Fig. 7b. The image shows very sharp facets parallel to {111} planes and a high degree of coherency between the matrix and the precipitates.

The composition of the small *Z* phase precipitates was investigated using an 18 nm diameter electron beam in the sample aged

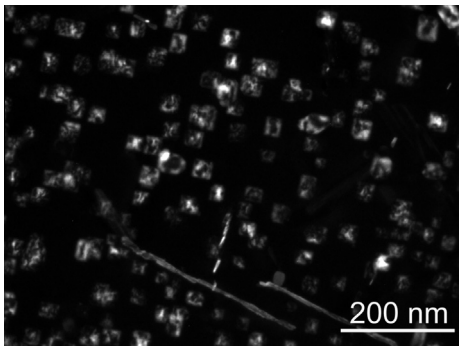

Fig. 8. Dark field image of small equiaxed precipitates from a 660 reflection after 1000 h ageing at 175 °C in alloy VE. The electron beam was near the [100] matrix zone axis.

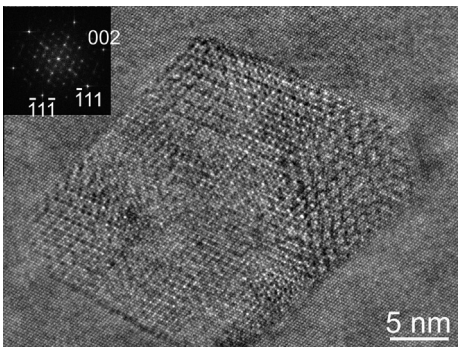

Fig. 9. High resolution image of a small sized precipitate along the [1 1 0] matrix zone axis, in alloy VE after 240 h at 175 °C. The diffractogram is shown.

for 1000 h. Fig. 10 shows three X-ray spectra obtained with the electron beam approximately parallel to the 0 0 1 zone axis, slightly tilted away to avoid dynamical diffraction effects. The spectra were obtained from an end-on *S* phase lath, a square shaped *Z* phase precipitate and the matrix. All three spectra show Cu, Mg and Al peaks. The strongest Mg signal is obtained from the *Z* phase precipitates, indicating a higher Mg:Cu ratio compared to the larger *S* phase particles. In order to estimate this ratio, the number of counts below the Mg K and Cu L lines was obtained from the spectra, after subtracting the background. The Cliff–Lorimer method [46] was applied, using the Mg/Cu ratio at an *S* phase precipitate, which is known to be equal to 1, as internal calibration. The Mg/Cu ratio of the *Z* phase precipitates was found to be about 2.

Fig. 11 shows the microstructure of the VE alloy after ageing at 240 °C for 240 h. Lath shaped *S* phase precipitates can be observed with a coarser distribution compared to that after ageing at 175 °C, but no *Z* phase precipitates. X-ray spectra obtained from an *S* phase precipitate and from the matrix are shown. The latter indicates the presence of Mg in solid solution.

3.3. Coincidence Doppler broadening of the annihilation radiation

In Fig. 12, the Δ curves plotted are those obtained for the artificial ageing stages labeled #1, #2 and #4 in Fig. 3. For sake of clarity, in the figure only three CDB curves are shown; i.e., the CDB curve corresponding to the ageing stage labeled #3 was omitted. Solid lines through the experimental data are the best-fit curves obtained following the procedure described in Section 2.3, using Eq. (1) and the Δ curves for positron trapping in vacancy-like defects in pure Al, Mg and Cu, shown in Fig. 2. The meaning of the different curves is analyzed below.

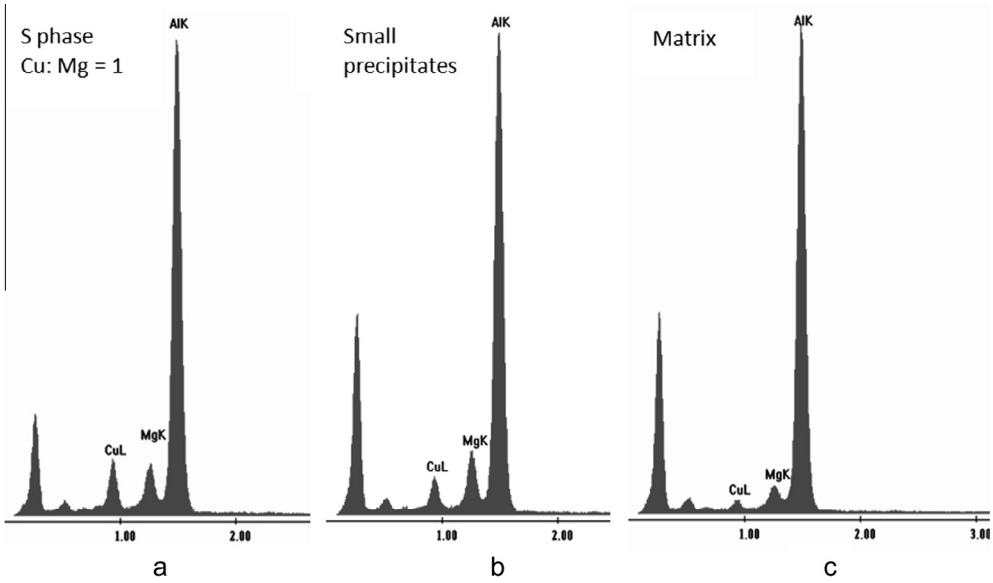

Fig. 10. Microanalysis results from alloy VE. (a) EDS spectrum from a *S* phase precipitate; (b) EDS spectrum from a *Z* phase precipitate; (c) EDS spectrum from the matrix close to the *S* phase and *Z* phase precipitates.

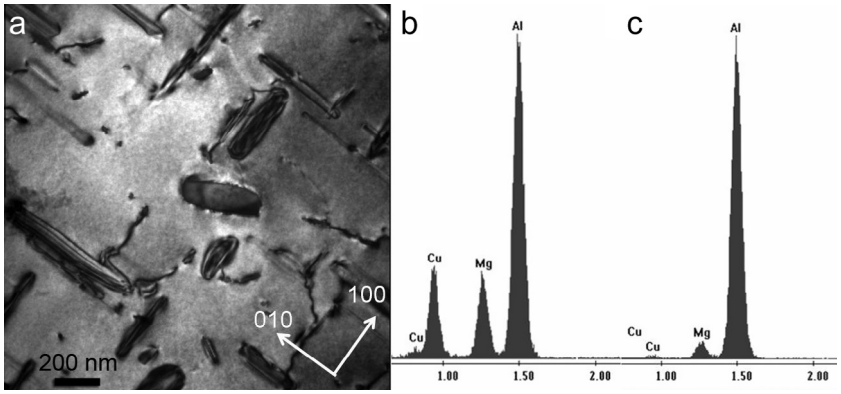

Fig. 11. (a) Microstructure of alloy VE after ageing at 240 °C for 240 h showing *S* phase precipitates. EDS spectra from an *S* phase precipitate (b) and the matrix (c).

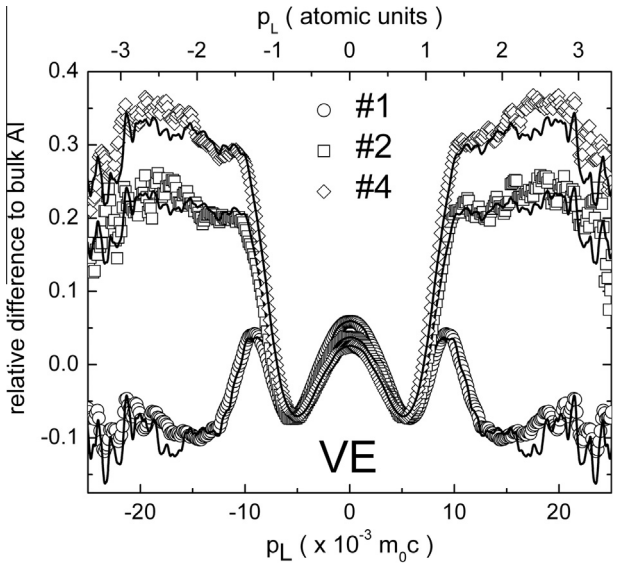

Fig. 12. CDB differences curves relative to well-annealed pure Al for alloy VE (Al–1.5 wt.%Cu–4.0 wt.%Mg). Labels #1, #2 and #4 represent selected ageing stages indicated in Fig. 3. Solid lines through the data are the result of the fitting procedure using reference spectra (see text). For sake of clarity, in the figure only three CDB curves are shown; i.e., the CDB curve corresponding to the ageing stage labeled #3 was omitted.

- VEA alloy (Al–1.5%Mg–4%Cu–0.5%Ag, wt.%).

3.4. Positron annihilation lifetime spectroscopy and hardness testing

The evolution of the Vickers hardness and positron lifetime during artificial ageing at 175 °C for samples of alloy VEA are shown in Fig. 13.

The addition of a small amount silver (equivalent to 0.12 at.%) to alloy VE promotes a significant increase in response to age hardening. Whereas the difference between the as-quenched and peak hardnesses for alloy VEA is 63 VHN, it is only 35 VHN for VE. Moreover, peak hardness of VEA is achieved after ageing for 110 h which is approximately half the time required for alloy VE. Softening of VEA during overageing is also less pronounced.

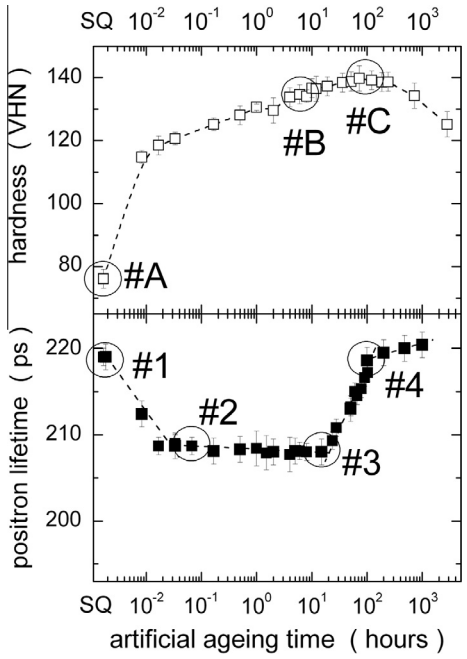

Fig. 13. Evolution during artificial ageing at 175 °C of the Vickers microhardness and positron lifetime for alloy VEA (Al–1.5 wt.%Cu–4.0 wt.%Mg–0.5 wt.%Ag). The dotted lines are only eye guides. Labels #A, #B and #C and #1, #2, #3 and #4 represent specific ageing stages selected to obtain TEM and CDB information (see text).

The evolution of the positron lifetime of VEA as a function of the artificial ageing is quite similar to that observed in alloy VE although the reduction of the initial lifetime value measured for as-quenched sample (~219 ps) was less marked. After ageing for 2 min, this value had fallen to 209 ps, after which it continued to decrease very slowly during the next 15 h. The lifetime then returned to a value of 219 ps after ageing for a time to reach peak hardness and continued to increase slowly during overageing. As with alloy VE, specific ageing stages that are indicated with circles labeled #A, #B, #C and #D on the hardness curve and those #1, #2, #3 and #4 on the lifetime evolution, were selected to obtain additional information by means of TEM and CDB.

3.5. Transmission electron microscopy

In contrast to the results of the VE alloy, precipitation in VEA only involved formation of the small equiaxed *Z* phase precipitates which were smaller in size than those observed in alloy VE (maximum diameter of 9 nm after prolonged ageing) and more finely dispersed. This accounts for the higher response to age hardening. Fig. 14 shows pairs of bright field and dark field images of the precipitates after ageing at 175 °C for 6 and 860 h. The size evolution is shown in Fig. 15. *S* phase precipitates were absent in the matrix and were only observed along the grain boundaries. Fig. 16 shows selected area diffraction patterns along the [0 1 1] and [2 1 1] zone axis where additional reflections due to the *Z* phase precipitates are shown and indexed, and a high resolution image obtained along the [0 1 1] matrix zone axis, where facets with the same characteristics as those described for the *Z* phase precipitates in alloy VE can be observed. Such facets could not be clearly observed at the early stages of ageing. The precipitates reflections in the diffraction pattern are identical to those shown in Fig. 7. The reflection used for the dark field images of Fig. 14 is indicated.

Fig. 17 shows the microstructure of the VEA alloy after ageing at 240 °C for 266 h. Larger sized *Z* phase precipitates were observed and occasionally *S* phase precipitates. In this figure are also shown X-ray spectra obtained from a *Z* phase precipitate and the matrix next to it. The spectra clearly show that the precipitate has a higher content of Mg and Cu as compared to the matrix. In addition, a small amount of Ag is observed in the precipitate spectrum. Comparison with the spectrum shown in Fig. 10 for the *Z* phase precipitates indicates that the proportion of Mg and Cu in the *Z* precipitates in the VEA alloy is qualitatively similar to that of *Z* precipitates in the VE alloy.

3.6. Coincidence Doppler broadening of the annihilation radiation

In Fig. 18, the Δ curves plotted are those obtained for the artificial ageing stages labeled #1, #2 and #4 in Fig. 13. As with alloy VE (Fig. 12), only three Δ curves for VEA are shown for the sake of clarity. Solid lines through the experimental data are the best-fit curves obtained in accordance with the procedure described in Section 2.3, using Eq. (1) and the Δ curves for positron trapping in vacancy-like defects in pure Al, Mg, Cu and Ag, shown in Fig. 2. The meaning of the different curves is analyzed below.

4. Discussion

4.1. Hardness and positron lifetime results

For both the VE and VEA alloys, the evolution of hardness and positron lifetime during artificial ageing reported in Figs. 3 and

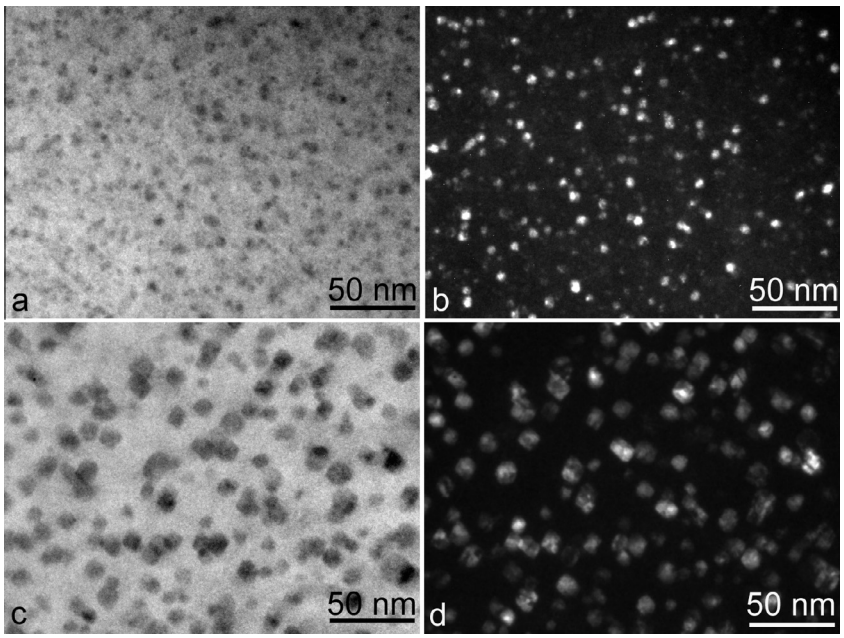

Fig. 14. Size evolution of precipitates in alloy VEA during ageing at 175 °C. (a and b) 6 h, (c and d) 860 h at 175 °C; (a and c) bright field images; (b and d) dark field images.

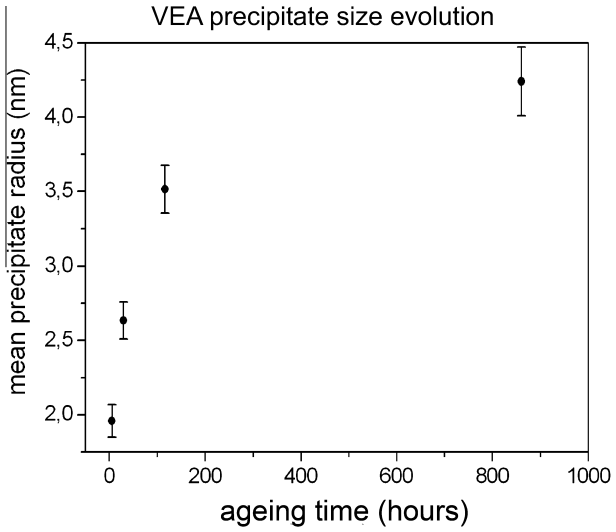

Fig. 15. Plot of the size evolution of *Z* phase precipitates in alloy VEA during ageing at 175 °C.

13 follows the same trend as that reported for other ternary Al–Cu–Mg alloys having lower Mg:Cu ratios [45] and also observed in more complex systems like the commercial alloys AA 2024 [41] and Al–5.6Cu–0.45Mg–0.45Ag–0.3Mn–0.18Zr (wt.%) [36].

In all the cases mentioned above, the evolution of hardness shows typically four stages: (i) initial rapid hardening, (ii) hardness plateau, (iii) secondary hardening and (iv) overageing. Microalloying additions of silver accelerate age hardening at 175 °C and significantly increase peak hardness. Moreover, the extended hardness plateau in the curve for alloy VE is much shortened, or practically eliminated in VEA. The present results agree with previous hardness measurements reported by Vietz and Polmear [5], although a short hardness plateau was observed in the Ag containing alloy. More recent results by Hirosawa et al. [47] in an alloy with similar composition also show the same trend, that is a shortening of the hardness plateau and higher hardness values. These effects are a consequence of the major change in the precipitation process caused by the Ag additions that will be discussed in Section 4.2.

The positron evolution results (Fig. 3) appear to display the classical behavior reported in PALS studies on age-hardenable Al-based

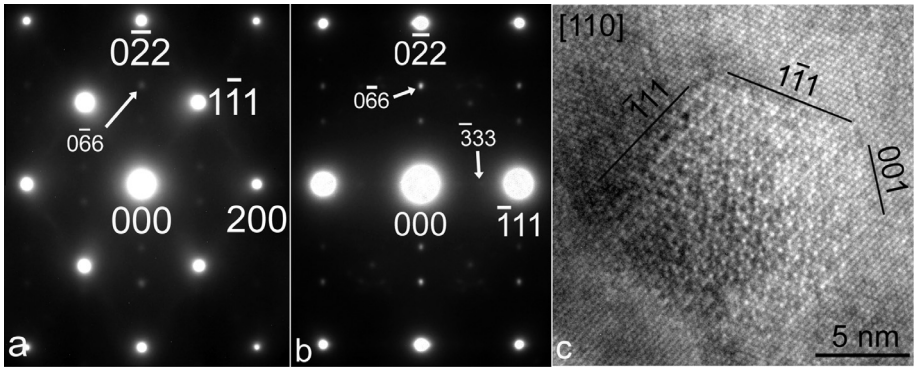

Fig. 16. Selected area diffraction patterns of alloy VEA after 116 h at 175 °C. (a) Matrix zone axis [1 1 0]; (b) matrix zone axis [2 1 1]. Weak reflections correspond to *Z* phase precipitates. The reflection used for the dark field images in Fig. 11 is indicated with an arrow in (a); (c) high resolution image of a precipitate after 860 h ageing at 175 °C in VEA alloy, showing facets parallel to the {1 1 1} and {1 0 0} type matrix planes.

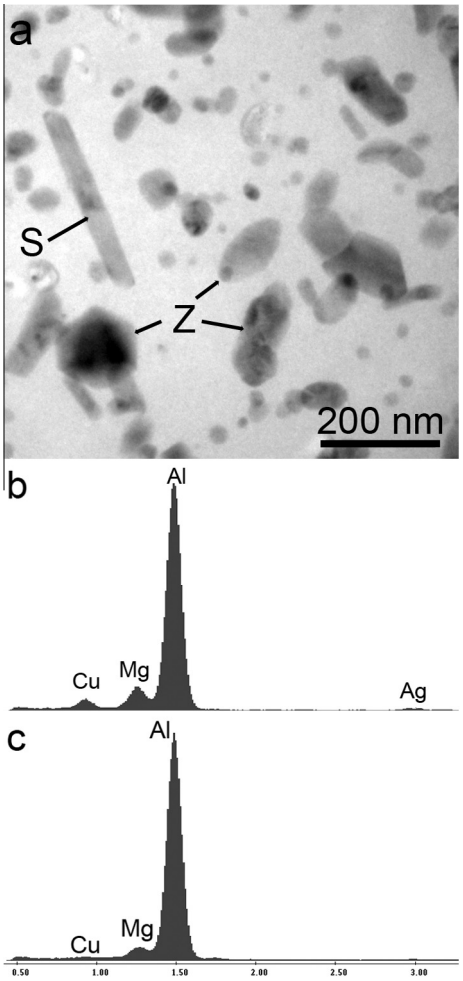

Fig. 17. VEA alloy aged for 266 h at 240 °C. (a) Bright field image close to the [1 1 1] matrix zone axis showing large sized *Z* phase precipitates, as compared to ageing at 175 °C and occasional *S* phase precipitates. (b and c) EDS results from a precipitate and the matrix, respectively, indicating a larger Mg, Cu and Ag content in the precipitate compared to the matrix.

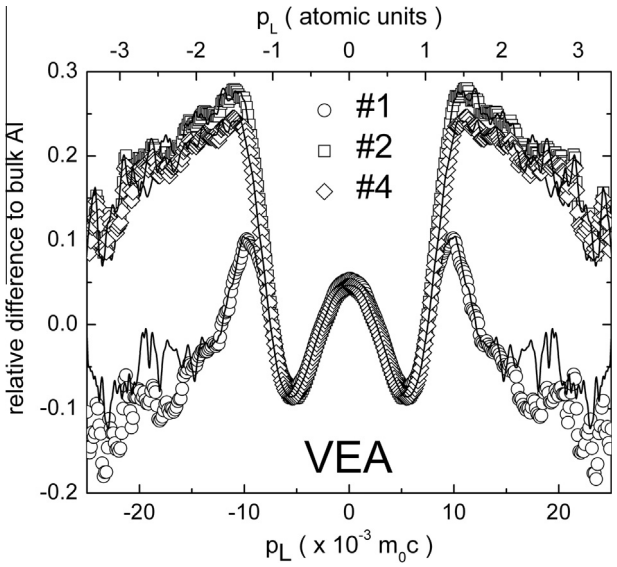

Fig. 18. CDB differences curves relative to well-annealed pure Al for alloy VEA (Al–1.5 wt.%Cu–4.0 wt.%Mg–0.5 wt.%Ag). Labels #1, #2 and #4 represent selected ageing stages indicated in Fig. 13. Solid lines through the data are the result of the fitting procedure using reference spectra (see text). For sake of clarity, in the figure only three CDB curves are shown; i.e., the CDB curve corresponding to the ageing stage labeled #2 was omitted.

alloys heat treated at temperatures above the Guinier–Preston zones solvus (for a review see reference [33]). The positron lifetime value for the silver-free alloy VE corresponding to the plateau in the evolution curve is higher than those reported for two other ternary Al–Cu–Mg alloys studied recently (Macchi et al. [45]). The compositions for these two alloys were:

Al–4Cu–0.3Mg (wt.%), with a Mg:Cu ratio equal to 0.075 (wt.%) and 0.20 (at.%); and
Al–2.5Cu–1.5Mg (wt.%) with a Mg:Cu ratio equal to 0.60 (wt.%) and 1.56 (at.%).

It has also been reported that these plateau values increase with increasing Mg:Cu ratios which indicates a progressive reduction in the fraction of Cu atoms in contact with vacancies as the Cu contents are decreased. For the VEA alloy, the significantly higher positron lifetime value in the plateau region (that is, that region in which positron lifetime has its minimum value) with respect to that measured for the VE alloy clearly confirms that silver has a significant effect as a microalloying element. It has been reported that the addition of silver to a ternary Al–Cu–Mg alloy promotes more vacancy-like defects to be retained after quenching and during ageing in these alloys [21,36]. These authors concluded that vacancies are strongly attracted by Ag-rich clusters formed during or immediately after cold water quenching from the solution treatment temperature [36]. It is the formation of these clusters that is thought to cause the rapid early hardening in the Al–Cu–Mg system [6].

4.2. Microstructural characterization by TEM

In the VE alloy, the microstructural characterization by TEM focused mainly on the later stages of ageing at 175 °C. The results indicate that *S*-phase laths grow during the second hardening stage at 175 °C, and that equiaxed *Z* phase precipitates are formed in between the *S*-phase laths. Since no dislocations appear to be associated with the latter precipitates, their formation is assumed to occur by homogeneous nucleation. A high coherency between the matrix and the precipitates was observed in high resolution images and very little strain contrast was observed surrounding the precipitates which also indicates a small misfit with respect to the matrix. Thus, the formation of these precipitates is expected to involve low interfacial and strain energies, and is consistent with homogeneous nucleation. The diffraction patterns of the precipitates are very similar to those corresponding to *Z* phase precipitates in the Ag-containing alloy of similar composition investigated by Chopra et al. [27,31], for which a large unit cell fcc structure was proposed. The orientation relationship (OR) was of cube–cube type and the morphology was shown to be octahedral with facets parallel to the {1 1 1} planes, occasionally cut by {1 0 0} type planes. In the paper by Chopra et al. [31], after a very long ageing at 240 °C, two variants of the *Z* precipitates were reported, one with cube–cube OR and the other in which the [0 1 1] *Z* phase zone axis is parallel to [1 1 1] matrix zone axis. In the present work, only the cube–cube OR was observed in the VE alloy. The composition results obtained with EDS in TEM indicate that the *Z* phase precipitates have a Mg/Cu ratio of about 2, larger than that for the *S* phase, where the Mg/Cu ratio is equal to 1.

After prolonged ageing at 240 °C the microstructure of alloy VE contained only *S* phase but no *Z* phase precipitates.

Previous work on Al–Cu–Mg alloys with high Mg:Cu ratios has mainly addressed the initial stages of precipitation during artificial

ageing and therefore the formation of *Z* phase precipitates was not observed [48–50]. However, the formation of small equiaxed precipitates in between *S* phase laths was reported by Hirosawa et al. [47] in an Al–1%Cu–3%Mg (wt.%) after ageing at 170 °C for 96 h. The precipitates were identified as *Z* phase and exhibited a cube–cube OR with the Al matrix. More recently, equiaxed precipitates in an Al–Cu–Mg alloy of the same composition as this work were reported to form during ageing at 200 °C [51]. The diffraction pattern of the precipitates show reflections identical to those reported in Fig. 7 of this work, that in turn coincide with those reported by Chopra et al. [31] and Hirosawa et al. [47]. However, these precipitates were incorrectly identified as corresponding to the *T* phase [51].

The results presented in this work indicate that in Al–Cu–Mg alloys with a high Mg:Cu ratio only *S* phase precipitates and *Z* phase precipitates are observed, the latter only below 240 °C, but no *T* phase precipitates.

In the VEA alloy, the addition of Ag was found to completely suppress the formation of *S* phase in favor of precipitates of the *Z* phase at 175 °C. Furthermore, the density of precipitates is much higher and the size was significantly smaller than that observed in the Ag free alloy. The maximum size of *Z* phase precipitates in the VEA alloy measured after 860 h was below 9 nm, while that of the VE alloy after 1000 h was 31 nm. This result indicates a smaller critical radius and larger nucleation rate of *Z* phase precipitates in VEA. Two effects may contribute to this. On one hand there is a larger solute supersaturation in the VEA alloy, since no solute was consumed by *S* phase precipitates, while on the other it is probable that the Ag additions may stimulate precipitate nucleation, as reported for alloys with lower Mg:Cu. The size evolution of the *Z* phase precipitates in VEA at 175 °C shows a steady increase with a decreasing growth rate with ageing time (see Fig. 15).

As for the *Z* precipitates in the VE alloy, only the cube–cube OR was observed by ageing at 175 °C in the VEA alloy. The reason only one variant is formed is that in precipitates with the cube–cube OR a high degree of coherence exists for all crystallographic directions, whereas for the other OR a high degree of coherence exists only for specific directions. Therefore, the nucleation of the variant with cube–cube OR is energetically favored.

According to the EDS spectrum in Fig. 17, the Mg:Cu ratio in the *Z* phase precipitates is similar to that obtained for alloy VE which was about 2. In addition, the *Z* precipitates in alloy VEA also contain Ag. This result agrees with EDS measurements of *Z* phase precipitates in Al–3%Mg–1%Cu–0.4%Ag, aged at 170 °C, where the ratio of Mg:Cu:Ag was found to be 6:3:1 [47]. In another 3DAP investigation on *Z* phase precipitates in an Al–Cu–Mg alloy with Si and Ag additions aged at 200 °C a Mg:Cu ratio of 1.75:1 was reported [52].

The striking effect of Ag additions on the microstructural evolution accounts for the significant difference of the hardness evolution of the two alloys studied in this work. While VE alloy exhibits a hardness plateau, during which the main microstructural features are *S* phase precipitates formed on dislocations, in the VEA alloy hardness grows steadily with ageing time, and reaches a higher peak value. This hardness evolution is due to a high density of *Z* phase precipitates that form already during the early stages of ageing and grow slowly with ageing time. The higher peak hardness is explained by the high density of *Z* phase precipitates. No evidence of any pre-precipitates such as GP zones was found. This can be explained by the high coherence of the cube–cube variant of the *Z* phase with the matrix.

4.3. Coincidence Doppler broadening of the annihilation radiation

- Alloy VE.

Table 1
Fractional concentrations C_i, also called contact probabilities, of the alloy components in contact with vacancy-like defects in alloy VE for different artificial ageing stages. These values were obtained by fitting the CDB differences curves using Eq. (1). F_{trap} is the trapping fraction of positrons annihilated in the alloy under the ageing conditions reported in the second column of the table.

Label	Ageing condition	Results obtained from the fitting of CDB experimental data			
		F_{trap} (%)	C_{Al} (%)	C_{Mg} (%)	C_{Cu} (%)
#1	As-quenched	51 ± 1	53 ± 2	27 ± 2	20 ± 2
#2	6 min @ 175 °C	58 ± 1	31 ± 2	27 ± 2	42 ± 2
#3	20 h @ 175 °C	60 ± 1	31 ± 2	29 ± 2	40 ± 2
#4	240 h @ 175 °C	55 ± 1	29 ± 2	36 ± 2	35 ± 2

Additional information on the positron traps is given by the chemical composition of their environment. To this aim, CDB differences curves obtained for the specific ageing conditions labeled # 1 to #4 in Fig. 3 (see second column of Table 1) were fitted using Eq. (1), where F_{trap} and the coefficients C^v_{Al}, C^v_{Cu}, and C^v_{Mg} were considered as adjustable parameters in the best-fit procedures. Solid lines represent the best fitting curves to the experimental data. The complementary percentage (100% – F_{trap}) represents the fraction of positrons annihilating in the VE alloy matrix. Fractional concentrations C^v_i, also called contact probabilities, of the alloy components in contact with vacancy-like defects are reported in the table and also plotted in Fig. 19.

From the analysis of the trapping fraction F_{trap} values for the different ageing stages studied, it can be concluded that about 50–60% of positrons are trapped and annihilated in solute–vacancy clusters or nanoprecipitates. The remaining positrons annihilate into the Al–Cu–Mg matrix. Despite there only are calculations on positron affinities to different pure elements [53], the existence of a competitive process for positron trapping between the alloy matrix and the solute–vacancy clusters formed in the alloys could be interpreted in terms of the "affinity concept" by which trapping sites are split into two states; i.e., matrix and clusters respectively.

The most important conclusions of the analysis of the results reported in Table 1 and Fig. 19 may be summarized as follows: (i) When comparing the atomic concentration in contact with vacancy-like defects C_i of the sample aged during 6 min at 175 °C with that of the as-quenched sample it can be seen that the

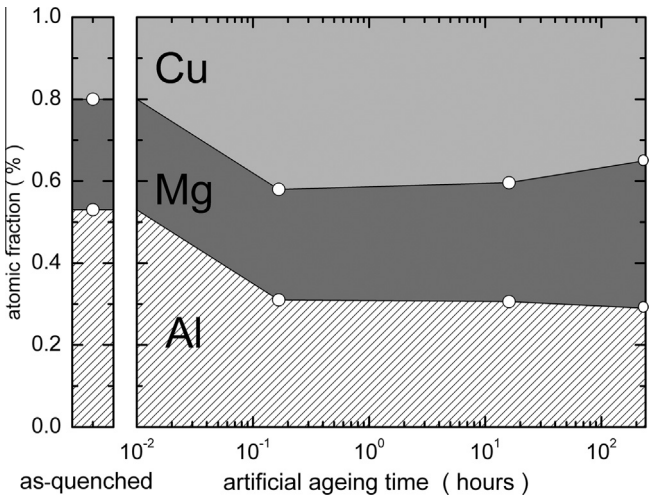

Fig. 19. Elemental fractions in contact with positron traps as a function of the ageing treatment at 175 °C for alloy VE (Al–1.5 wt.%Cu–4.0 wt.%Mg). Fractional concentrations C_i for selected ageing stages pointed out with open white circles were obtained from the best fitting curve (Al, Mg and Cu in contact with vacancy-like defects using Eq. (1)). Estimated statistical scatter: 0.5%.

Table 2
Fractional concentrations C_i, also called contact probabilities, of the alloy components in contact with vacancy-like defects in alloy VEA for different artificial ageing stages. These values were obtained by fitting the CDB differences curves using Eq. (1). F_{trap} is the trapping fraction of positrons annihilated in the alloy under the ageing conditions reported in the second column of the table.

Label	Ageing condition	Results obtained from the fitting of CDB experimental data				
		F_{trap} (%)	C_{Al} (%)	C_{Mg} (%)	C_{Cu} (%)	C_{Ag} (%)
#1	As-quenched	58 ± 1	52 ± 2	23 ± 2	15 ± 2	10 ± 2
#2	10 min @ 175 °C	66 ± 1	27 ± 2	36 ± 2	27 ± 2	10 ± 2
#3	15 h @ 175 °C	65 ± 1	27 ± 2	35 ± 2	28 ± 2	10 ± 2
#4	72 h @ 175 °C	62 ± 1	23 ± 2	42 ± 2	25 ± 2	10 ± 2

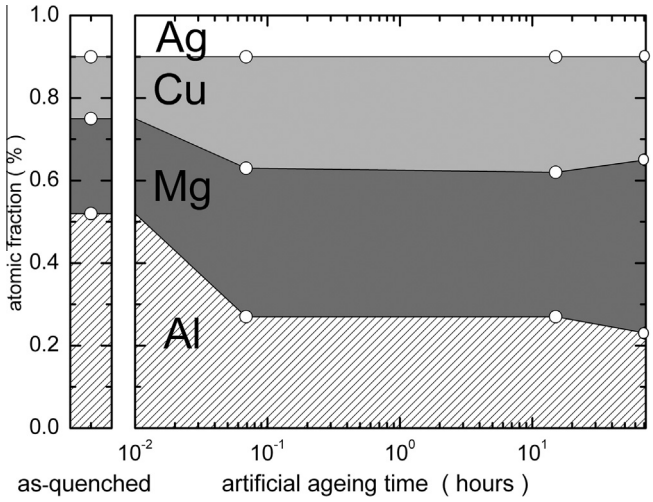

Fig. 20. Elemental fractions in contact with positron traps as a function of the ageing treatment at 175 °C of alloy VEA (Al–1.5 wt.%Cu–4.0 wt.%Mg–0.5 wt.%Ag). Fractional concentrations C_i for selected ageing stages pointed out with open white circles were obtained from the best fitting curve (Al, Mg, Cu and Ag in contact with vacancy-like defects using Eq. (1)). Estimated statistical scatter 0.5%.

amount of Al strongly diminishes, the Mg content remains constant and the Cu content shows a sharp increase (about 100%); (ii) for an intermediate ageing time, coincident with the end of the lifetime plateau C_{Al} remains constant. Furthermore, a small increase of the Mg content accompanied by an equivalent decrease of the amount of Cu is observed; and (iii) for longer ageing times (CDB data corresponding to the sample aged 240 h at 175 °C against that aged 20 h at 175 °C), the Al content slightly decreases while the amount of Mg significantly increases in about 20%. Conversely, the Cu content decreases in more than 10%. Furthermore, it is worth mentioning that in alloy VE, when it is submitted to artificial ageing for different times, the C_{Mg}/C_{Cu} ratio varies from approximately 0.6 to 1. Specifically, in the region of peak age hardening, a quantitative estimate of the solute fractions around vacancies that are associated with nanoparticles indicates a Mg:Cu ratio of 1.

- VEA alloy.

For this alloy, additional information was also obtained on the positron traps particularly regarding the chemical composition of their environment. So, CDB differences curves obtained for the specific ageing conditions labeled #1 to #4 in Fig. 13 (see second column of Table 2) were fitted using Eq. (1) considering F_{trap} and the coefficients C^v_{Al}, C^v_{Cu}, C^v_{Mg}, and C^v_{Ag} as adjustable parameters in the best-fit procedures. Solid lines represent the best fitting curves to the experimental data. The results obtained from the fitting procedure, are reported in Table 2 and Fig. 20.

The trapping fraction F_{trap} values for the different ageing stages studied indicate that between approximately 55% and 65% of positrons are trapped and annihilated in nano- or sub-nanometric solute–vacancy aggregates. The remaining positrons annihilate into the Al–Cu–Mg–Ag matrix. A systematic increase of F_{trap} is observed for alloy VEA when comparing with those values of alloy VE for similar ageing stages of both alloys.

These results allow us to conclude that: (i) The silver content remains the same during all stages of ageing; (ii) when comparing the C_i values for the VEA sample aged during 10 min at 175 °C with that of the as-quenched sample, it can be seen that the amount of Al strongly diminishes, the Mg content increase in about 50%, and the Cu content also increases in 50% ca.; (iii) at the end of the lifetime plateau, all the solute fractional concentrations remain constant; and (iv) for a further ageing time, the Al content slightly decreases, the Mg content increases in about 20% and the amount of Cu remains almost constant (a slight decrease is observed).

Since the fraction of silver atoms around vacancies associated with solute–vacancy clusters or nanoprecipitates is constant, it is particularly interesting to analyze the changes in the C_{Mg}/C_{Cu} ratios in the case of the artificially aged samples. The value of this parameter is about 1.3 for the intermediate artificial ageing stage and increases to 1.7 around peak ageing. This value is almost the double to that obtained for alloy VE indicating that the addition of Ag as microalloying element, results in a larger fractional concentration of Mg solute atoms surrounding vacancy-like defects.

The present results agree with previous findings in an Al–Cu–Mg alloy with high Mg:Cu ratio and Ag additions using 3DAP, where clusters containing Cu, Mg and Ag atoms have been reported to form during the early stages of ageing at 170 °C [47], and show that such clusters are vacancy–solute complexes.

Finally, the CDB results allow the interpretation of the positron lifetime evolution shown in Figs. 3 and 13. In both alloys, the initial decrease is related to the increase in the Cu content surrounding vacancy-like defects, while the strong increase in positron lifetime beyond the plateau is related to the increase in the Mg content decorating the vacancy-like defects. The differences between the CDB results in VE and VEA alloys indicate that in the VE alloy, positrons annihilate mainly at *S* phase laths, since for long ageing times the ratio of Mg:Cu atoms around vacancies is about 1, while in the VEA alloy positron annihilation is related to the precipitation of the *Z* phase, with a higher Mg:Cu ratio.

5. Conclusions

A combination of the experimental techniques TEM, Positron Annihilation Lifetime Spectroscopy, and Coincidence Doppler Broadening has been used to provide more understanding of the effects of a microalloying addition of Ag on the precipitation processes in the alloy Al–1.5%Cu–4.0%Mg which has a high Mg:Cu ratio.

The main conclusions from these studies are as follows:

1. Results for both ternary and quaternary alloys indicate that, immediately after quenching from the solution treatment temperature, and for very short ageing times at 175 °C, vacancy–solute (Cu, Mg) and vacancy–solute (Cu, Mg, Ag) clusters are formed, respectively. CDB positron results show that Ag causes a greater density of vacancies to be retained by quenching. Furthermore, from PALS results it can be concluded that during this early artificial ageing stage solute transport mechanisms appear to be similar. This behavior is analogous to what has been exclusively observed by PALS in other alloys based on the Al–Cu–Mg system and accounts for the rapid early hardening that occurs in these alloys.

2. Studies of the ternary alloy confirm that prolonged ageing at 175 °C leads to precipitation of an uniform, but relatively coarse dispersion of the *Z* phase in the matrix in between helical dislocations decorated with particles of the well known *S* phase (Al_2–Cu–Mg). The *Z* phase is octahedral in shape and high resolution microscopy has revealed it is highly coherent with the aluminum matrix. It has a cubic structure that contains Mg and Cu in the approximate ratio of 2:1 that distinguishes it from the complex cubic *T* phase (Al_6CuMg_4) which is shown in the generally accepted Al–Cu–Mg phase diagram. The *S* phase is still present in the ternary alloy aged at 240 °C whereas the *Z* and *T* phases are both absent.
3. The addition of small amounts of Ag suppresses formation of the *S* phase and stimulates precipitation of a denser dispersion of smaller precipitates of the *Z* phase on ageing at 175 °C which accounts for the greater response of the quaternary alloy to age hardening. Ag also increases the stability of the *Z* phase so that it remains present after prolonged ageing at 240 °C. Once again the *T* phase was not observed after ageing the quaternary alloy at 175 or 240 °C.
4. Comparing the CDB results with the positron lifetime evolution suggests that the initial decrease in the latter during ageing of both alloys can be attributed to the increase of Cu atoms in contact with vacancies. To the contrary, the strong increase in positron lifetime in both alloys that follows on further ageing can be attributed to the progressive enrichment of magnesium atoms in contact with vacancies probed by positrons, as indicated by the CDB results. Finally, for long ageing times: (i) in the ternary alloy, the ratio of Mg to Cu atoms around vacancies was found to equal 1 suggesting that positrons annihilate mainly at *S* phase laths; and (ii) in the Ag added alloy the ratio of Mg:Cu atoms in contact with vacancies was found to be around 2 accounting for positron annihilation at *Z* phase precipitates.
5. No evidence was obtained that a pre-precipitate such as GP zones preceded formation of the *Z* phase in either alloy.

Acknowledgments

This work was partially supported by Agencia Nacional de Promoción Científica y Tecnológica (Argentina) (PICT 2011-1088 and PICT 2011-0643), Consejo Nacional de Investigaciones Científicas y Técnicas (Argentina) (PIP #112-201101-00793), Comisión de Investigaciones Científicas de la Provincia de Buenos Aires and SECAT (UNCPBA) and Secretaría de Ciencia, Técnica y Posgrado, Universidad Nacional de Cuyo (C6/C461).

References

[1] A. Wilm, German Patent DRP 244554 (1909).
[2] G.B. Brook, Precipitation in metals, Special Report N. 3, Fulmer Research Institute, UK, 1963.
[3] H.K. Hardy, The ageing characteristics of some ternary aluminium–copper–magnesium alloys with copper:magnesium ratios of 7:1 and 2.2:1, J. Inst. Met. 83 (1954–55) 17–34.
[4] I.J. Polmear, The effects of small additions of silver on the aging of some aluminium alloys, Trans. Met. Soc. AIME 230 (1964) 1331.
[5] J.T. Vietz, I.J. Polmear, The influence of small additions of silver on the ageing of aluminium alloys: observations on Al–Cu–Mg alloys, J. Inst. Met. 94 (1966) 410–419.
[6] S.P. Ringer, T. Sakurai, I.J. Polmear, Origins of hardening in aged Al–Cu–Mg–(Ag) alloys, Acta Mater. 45 (1997) 3731–3744.
[7] V. Gerold, H. Haberkorn, Roentgengraphische Untersuchung der Kaltaushaertung von Aluminium–Magnesium–Kupfer und Aluminium–Magnesium–Zink Leguierungen, Z. Metallk. 50 (1959) 568–576.
[8] J.M. Silcock, The structural ageing characteristics of Al–Cu–Mg alloys with copper:magnesium weight ratios of 7:1 and 2.2:1, J. Inst. Met. 89 (1960–61) 203–210.
[9] S.P. Ringer, K. Hono, T. Sakurai, I.J. Polmear, Cluster hardening in an aged Al–Cu–Mg alloy, Scr. Mater. 36 (1997) 517–521.
[10] R.N. Wilson, P.G. Partridge, The nucleation and growth of *S′* precipitates in an aluminium–2.5% copper–1.2% magnesium alloy, Acta Metall. 13 (1965) 1321–1327.
[11] G.C. Weatherly, R.B. Nicholson, An electron microscope investigation of the interfacial structure of semi-coherent precipitates, Philos. Mag. A 17 (1968) 801–831.
[12] A.K. Gupta, P. Gaunt, M.C. Chaturvedi, The crystallography and morphology of the *S′* phase precipitate in an Al(CuMg) alloy, Philos. Mag. A 55 (1987) 375–387.
[13] G. Sha, R.K.W. Marceau, S.P. Ringer, Precipitation and solute clustering in aluminium: advanced characterisation techniques, in: R.N. Lumley (Ed.), Fundamentals of Aluminium Metallurgy, Woodhead Publishing, Cambridge, 2011, pp. 345–366.
[14] F. Cuisiat, P. Duval, R. Graf, Etude des premiers stades de decomposition d́un alliage Al–Cu–Mg, Scr. Metall. 18 (1984) 1051–1056.
[15] N. Sen, D.R.F. West, The Mechanism of Phase Transformations in Crystalline Solids, Monograph and Report Series, No. 33, Institute of Metals, London, 1969.
[16] R.J. Chester, I.J. Polmear, TEM investigation of precipitates in AlCuMgAg and AlCuMg alloys, Micron 11 (1980) 311–312.
[17] K.M. Knowles, W.M. Stobbs, The structure of 1 1 1 age-hardening precipitates in Al–Cu–Mg–Ag alloys, Acta Crystallogr. B 44 (1988) 207–227.
[18] B.C. Muddle, I.J. Polmear, The precipitate Ω phase in Al–Cu–Mg–Ag alloys, Acta Metall. 37 (1989) 777–789.
[19] K. Hono, T. Sakurai, I.J. Polmear, Pre-precipitate clustering in an AlCuMgAg alloy, Scr. Metall. Mater. 30 (1994) 695–700.
[20] S.P. Ringer, K. Hono, I.J. Polmear, T. Sakurai, Nucleation of precipitates in aged Al–Cu–Mg–(Ag) alloys with high Cu:Mg ratios, Acta Metall. 44 (1996) 1883–1898.
[21] A. Somoza, A. Dupasquier, I.J. Polmear, P. Folegati, R. Ferragut, Positron-annihilation study of the ageing kinetics of AlCu-based alloys. II. Ag microalloying, Phys. Rev. B 61 (2000) 14464–14469.
[22] K. Hono, N. Sano, S.S. Babu, R. Okano, T. Sakurai, Atom probe study of the precipitation process in AlCuMgAg alloys, Acta Metall. 41 (1993) 829–838.
[23] L. Reich, M. Murayama, K. Hono, Evolution of Ω phase in al Al–Cu–Mg–Ag alloy – a three dimensional atom probe study, Acta Mater. 46 (1998) 6053–6062.
[24] C.R. Hutchinson, X. Fan, S.J. Pennycook, G.J. Shiflet, On the origin of the high coarsening resistance of Ω plates in Al–Cu–Mg–Ag alloys, Acta Mater. 49 (2001) 2827–2841.
[25] I.J. Polmear, M.J. Couper, Design and development of an experimental wrought aluminum alloy for use at elevated temperatures, Metall. Trans. 19A (1988) 1027–1035.
[26] I.J. Polmear, G. Pons, Y. Barbaux, H. Octor, C. Sanchez, A.J. Morton, W.E. Borbidge, S. Rogers, After concorde: evaluation of creep resistant Al–Cu–Mg–Ag alloys, Mater. Sci. Technol. 15 (1999) 861–868.
[27] H.D. Chopra, K.J. Liu, B.C. Muddle, I.J. Polmear, The structure of metastable 111 precipitates in an Al–2.5 wt.% Cu–1.5 wt.% Mg–0.5 wt.% Ag alloy, Philos. Mag. Lett. 71 (1995) 319–324.
[28] G. Bergman, J.T.L. Waugh, L. Pauling, Crystal structure of the intermetallic compound $Mg_{32}(Al, Zn)_{49}$ and related phases, Nature 169 (1957) 1057–1058.
[29] G. Bergman, J.T.L. Waugh, L. Pauling, The crystal structure of the metallic phase $Mg_{32}(Al, Zn)_{49}$, Acta Crystallogr. 10 (1957) 254–259.
[30] J.H. Auld, J.T. Vietz, I.J. Polmear, T-phase precipitation induced by the addition of silver to an aluminium–copper–magnesium alloy, Nature 209 (1966) 703–704.
[31] H.D. Chopra, B.C. Muddle, I.J. Polmear, The structure of primary strengthening precipitates in an Al–1.5 wt.% Cu–4.0 wt.%Mg–0.5 wt.% Ag alloy, Philos. Mag. Lett. 73 (1996) 351–357.
[32] A. Dupasquier, G. Kögel, A. Somoza, Studies of light alloys by positron annihilation techniques, Acta Mater. 52 (2004) 4707–4726.
[33] A. Somoza, A. Dupasquier, Vacancies in aluminium and solute–vacancy interactions in aluminium alloys, in: R.N. Lumley (Ed.), Fundamentals of Aluminium Metallurgy, Woodhead Publishing, Cambridge, 2011, pp. 386–421.
[34] A. Somoza, M.P. Petkov, K.G. Lynn, A. Dupasquier, Stability of vacancies during solute clustering in Al–Cu-based alloys, Phys. Rev. B 65 (094107) (2002) 1–6.
[35] A. Calloni, A. Dupasquier, R. Ferragut, P. Folegati, M.M. Iglesias, I. Makkonen, M. Puska, Positron localization effects on the Doppler broadening of the annihilation line: aluminum as a case study, Phys. Rev. B 72 (054112) (2005) 1–6.
[36] R. Ferragut, A. Dupasquier, C.E. Macchi, A. Somoza, R.N. Lumley, I.J. Polmear, Vacancy–solute interactions during multiple-step ageing of an Al–Cu–Mg–Ag alloy, Scr. Mater. 60 (2009) 137–140.
[37] R.K.W. Marceau, G. Sha, R. Ferragut, A. Dupasquier, S.P. Ringer, Solute clustering in Al–Cu–Mg alloys during the early stages of elevated temperature ageing, Acta Mater. 58 (2010) 4923–4939.
[38] R. Ferragut, Atomic fraction around defects associated with nanoparticles in Al–Cu–Mg alloys, Physica B 407 (2012) 2676–2683.
[39] Y. Nagai, M. Murayama, Z. Tang, T. Nonaka, K. Hono, M. Hasegawa, Role of vacancy–solute complex in the initial rapid age hardening in an Al–Cu–Mg alloy, Acta Mater. 49 (2001) 913–920.
[40] G. Dlubek, P. Lademann, H. Krause, S. Krause, R. Unger, Positron lifetime studies of decomposition in 2024 (Al–Cu–Mg) and 7010 (Al–Zn–Cu–Mg) alloys, Scr. Mater. 39 (1998) 893–899.
[41] R. Ferragut, A. Somoza, Positron, age-hardening and precipitation in predeformed 2024 (Al–Cu–Mg) alloy, Phys. Status Sol. (a) 175 (1999) R1–R2.

[42] T.E.M. Staab, E. Zschech, R. Krause-Rehberg, Positron lifetime measurements for characterization of nano-structural changes in the age hardenable AlCuMg 2024 alloy, J. Mater. Sci. 35 (2000) 4667–4672.
[43] M. Massazza, G. Riontino, A. Dupasquier, P. Folegati, R. Ferragut, A. Somoza, Secondary ageing in Al–Cu–Mg, Philos. Mag. Lett. 82 (2002) 495–502.
[44] P. Kirkegaard, N.J. Pedersen, M. Eldrup, PATFIT-88: A Data-Processing System for Positron Annihilation Spectra on Mainframe and Personal Computers, M-2740, Risø National Laboratory, DK-4000 Roskilde, Denmark, 1989.
[45] C. Macchi, A. Somoza, R. Ferragut, A. Dupasquier, I.J. Polmear, Ageing processes in Al–Cu–Mg alloys with different Cu/Mg ratios, Phys. Status Sol. (c) 6 (2009) 2322–2325.
[46] G. Cliff, G.W. Lorimer, The quantitative analysis of thin specimens, J. Microsc. 103 (1975) 203–207.
[47] S. Hirosawa, T. Omura, Y. Suzuki, T. Sato, Improvement of bake-hardening response of Al–Mg–Cu alloys by means of nanocluster assist processing (NCAP) technique, Mater. Sci. Forum 519–521 (2006) 215–220.
[48] P. Ratchev, B. Verlinden, P. Van Houtte, S' phase precipitation in Al–4 wt.% Mg–1 wt.% Cu alloy, Scr. Metall. Mater. 30 (1994) 599–604.
[49] P. Ratchev, B. Verlinden, P. de Smet, P. Van Houtte, Effect of cooling rate and predeformation on the precipitation hardening of an Al–4.2 wt.% Mg–0.6 wt.% Cu alloy, Scr. Mater. 38 (1998) 1195–1201.
[50] P.I. Gouma, D.J. Lloyd, M.J. Mills, Precipitation processes in Al–Mg–Cu alloys, Mater. Sci. Eng. A 319–321 (2001) 439–442.
[51] Z. Chen, J. Zhang, J. Shu, G. Sha, J. Xia, S. Wang, S.P. Ringer, Effects of Si addition on the microstructure evolution of Al–Cu–Mg alloys in the alpha + S + T phase field, Philos. Mag. Lett. 93 (2013) 648–654.
[52] C. Li, G. Sha, B. Gun, J.H. Xia, X.F. Liu, Y.Y. Wu, N. Birbilis, S.P. Ringer, Enhanced age-hardening response of Al–4 Mg–1 Cu (wt.%) microalloyed with Ag and Si, Scr. Mater. 68 (2013) 857–860.
[53] R.M. Nieminen, Electronic structure and positron spectroscopy of solids and surfaces, in: A. Dupasquier, A.P. Mills Jr. (Eds.), Positron Spectroscopy of Solids, IOS Press, Amsterdam, 1995, pp. 448–490.